JACS
JOURNAL OF THE AMERICAN CHEMICAL SOCIETY

Article

pubs.acs.org/JACS

Optokinetically Encoded Nanoprobe-Based Multiplexing Strategy for MicroRNA Profiling

Sungi Kim, Jeong-Eun Park, Woosung Hwang, Jinyoung Seo, Young-Kwang Lee,[†] Jae-Ho Hwang, and Jwa-Min Nam*

Department of Chemistry, Seoul National University, Seoul 08826, South Korea

Supporting Information

ABSTRACT: Multiplexed real-time analysis on multiple interacting molecules and particles is needed to obtain information on binding patterns between multiple ligands and receptors, specificity of bond formations, and interacting pairs in a complex medium, often found in chemical and biological systems, and difference in binding affinity and kinetics for different binding pairs in one solution. In particular, multiplexed profiling of microRNA (miRNA) in a reliable, quantitative manner is of great demand for the use of miRNA in cell biology, biosensing, and clinical diagnostic applications, and accurate diagnosis of cancers with miRNA is not possible without detecting multiple miRNA sequences in a highly specific manner. Here, we report a multiplexed molecular detection strategy with optokinetically (OK) coded nanoprobes (NPs) that show high photostability, distinct optical signals, and dynamic behaviors on a supported lipid bilayer (SLB) (OK-NLB assay). Metal NPs with three distinct dark-field light scattering signals [red (R), green (G), and blue (B)] and three different target miRNA half-complements were tethered to a two dimensionally fluidic SLB with mobile (M) or immobile (I) state. *In situ* single-particle monitoring and normalized RGB analysis of the optokinetically combinatorial assemblies among three M-NPs and three I-NPs with dark-field microscopy (DFM) allow for differentiating and quantifying 9 different miRNA targets in one sample. The OK-NP-based assay enables simultaneous detection of multiple miRNA targets in a highly quantitative, specific manner within 1 h and can be potentially used for diagnosis of different cancer types. We validated the OK-NLB assay with single-base mismatched experiments and HeLa cell-extracted total RNA samples by comparing the assay results to the quantitative reverse transcription polymerase chain reaction (qRT-PCR) results.

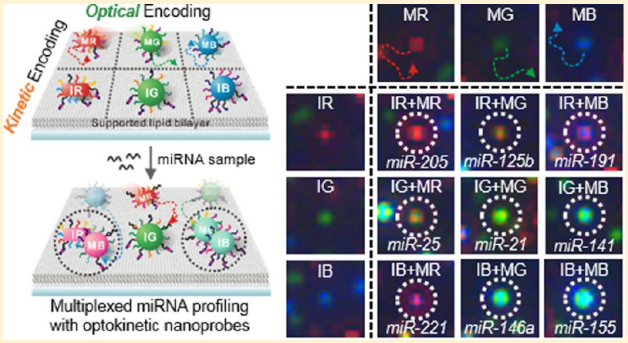

INTRODUCTION

Multiparallel reactions among a variety of reactants are common phenomena in chemical and biological systems.[1−3] Simultaneous interpretation of multiple interactions from complex reaction mixtures offers important chemical or biological information including binding affinity and nature, reaction mechanisms, reaction and binding specificity, biodiagnostics, and rapid screening in biological sensing.[4] It is, however, challenging to distinguish multiple interactions in a single reaction mixture due to the lack of tools for obtaining reliable information on complex binding events and their kinetic information with multiple (or multiplexed) readouts.[5]

MicroRNAs (miRNAs) are small (~22-nt), single stranded, noncoding RNAs. miRNAs act as post-transcriptional gene regulators and have emerged as potential diagnostic and prognostic biomarkers for human diseases including cancers and neurodegenerative diseases.[6−8] The capability to identify and quantify multiple miRNA species is critical in translating miRNA sequences into useful information and is highly beneficial for improving the accuracy, precision, and specificity of diagnosis.[9] Accurate quantification of miRNA is, however, difficult due to its intrinsically short length and instability.[10] Although the quantitative reverse transcription polymerase chain reaction (qRT-PCR) offers high sensitivity and specificity, it requires poly-A tail or specially designed primer in cDNA formation and error-prone enzymatic amplification and is relatively low-throughput.[11] Microarrays are high-throughput, but they use fluorescence-based quantification that provides only relative expression values.[11] Recently, researchers have developed nanostructure-based miRNA detection methods that use biobarcode amplification,[12] nanopores,[13] gold nanoparticles,[14] scanometric arrays,[15] silicon nanowires,[16] graphene oxide,[17] and quantum dots.[18] However, previously reported nanostructure-based assays have limited multiplexing and quantification capabilities, and the assay time is typically well over 1 h with complicated multiple reaction steps and setups. Further, fluorescence-based methods including PCR and microarrays have limitations in photostability and multiplexing capability of fluorophore probes.

Received: February 7, 2017
Published: February 9, 2017

DOI: 10.1021/jacs.7b01311
J. Am. Chem. Soc. 2017, 139, 3558−3566

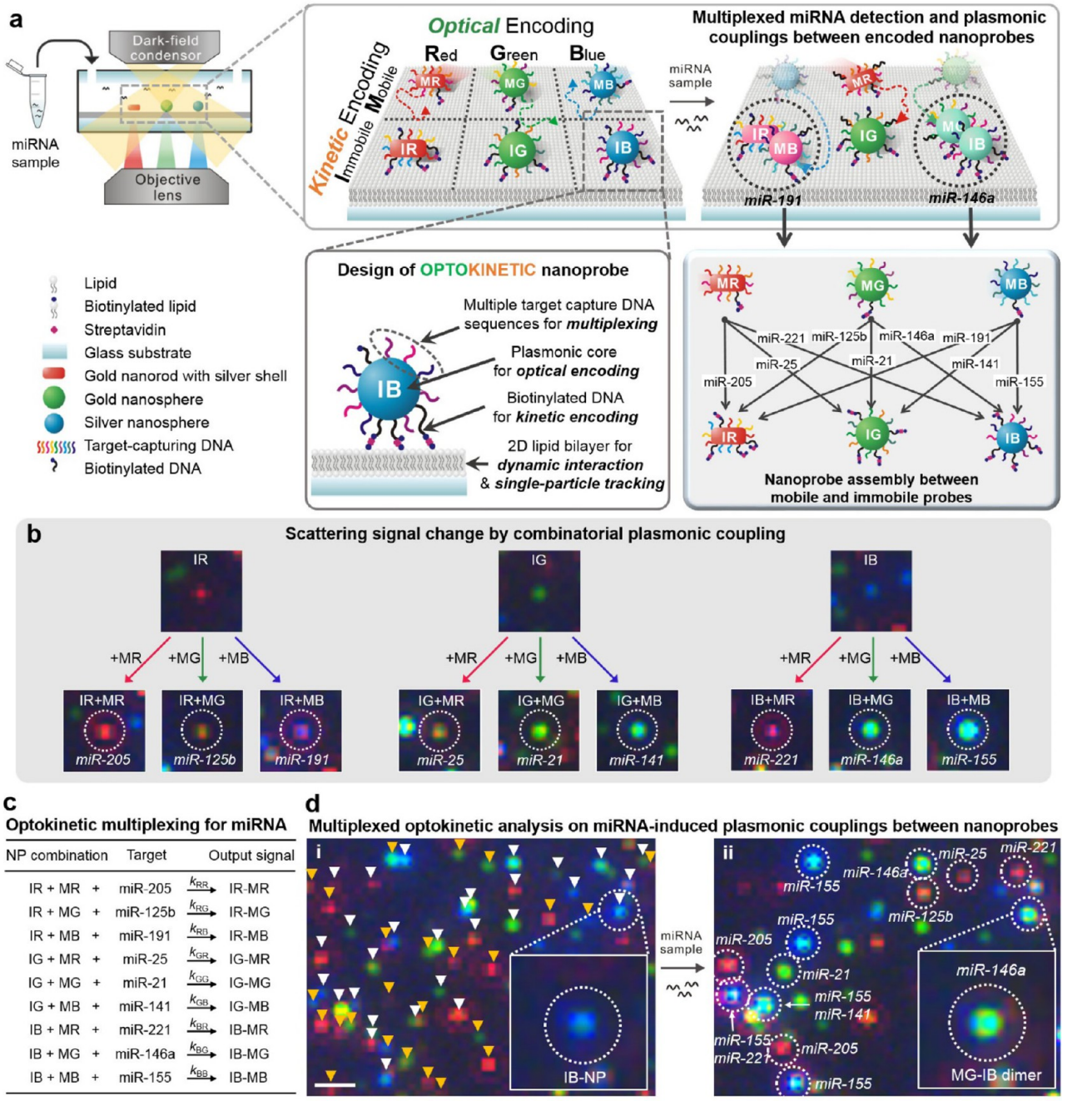

NP combination		Target		Output signal
IR + MR	+	miR-205	k_{RR}	IR-MR
IR + MG	+	miR-125b	k_{RG}	IR-MG
IR + MB	+	miR-191	k_{RB}	IR-MB
IG + MR	+	miR-25	k_{GR}	IG-MR
IG + MG	+	miR-21	k_{GG}	IG-MG
IG + MB	+	miR-141	k_{GB}	IG-MB
IB + MR	+	miR-221	k_{BR}	IB-MR
IB + MG	+	miR-146a	k_{BG}	IB-MG
IB + MB	+	miR-155	k_{BB}	IB-MB

Figure 1. Optokinetically encoded nanoprobe (OK-NP)-tethered supported lipid bilayer (SLB) assay (OK-NLB assay). (a) The miRNA sample is directly injected into a reaction chamber, and NP interactions are monitored with dark-field microscopy (DFM). Six types of OK-NPs are prepared by kinetic [mobile (M) and immobile (I)] and optical [red (R), green (G), and blue (B)] coding methods. OK-NPs are composed of plasmonic nanoparticle core, multiple target capture DNAs, and biotinylated DNA. The NP assembly events between the M-NPs and the I-NPs are mediated by target miRNAs and identified with scattering color changes via plasmonic coupling. The nineplexing strategy using combinatorial assemblies between OK-NPs relies on each assembly mode, which was mediated by 9 different target miRNAs (bottom right). (b) Nine different scattering signal changes due to combinatorial plasmonic couplings induced by M-NPs binding to I-NPs. (c) Nine NP assembly reaction equations are described as multicomponent association reactions. (d) DFM images of DF scattering signals from individual OK-NPs on SLB. (d) (i) OK-NP identification by particle color and mobility. White and orange solid triangles indicate I-NPs and M-NPs, respectively. (ii) Multiplexed combinations of OK-NP assemblies reveal the target miRNA-induced particle assemblies in highly parallel manner (white dashed circles). The scale bar is 2 μm.

Therefore, it remains challenging to develop a miRNA identification and quantification method that meets both speed and multiplexed detection requirements.

Here, we developed an optokinetically encoded plasmonic nanoprobe-based multiplexing strategy, and this strategy was used for miRNA profiling to identify and quantify 9 different miRNA species simultaneously on two-dimensional (2D) supported lipid bilayer (SLB) (Figure 1). The nanoprobes (NPs) here are coded optically (combinatorial plasmonic couplings) and kinetically (particle mobility) to generate highly multiplexed detection of targets (Figure 1). In DNA design, first, three different oligonucleotide sequences for detecting three different miRNA sequences and biotinylated DNA for tethering NPs to biotinylated SLB via streptavidins were

DOI: 10.1021/jacs.7b01311
J. Am. Chem. Soc. 2017, 139, 3558−3566

modified to each NP. The number of modified biotinylated DNA strands per particle determines the mobility of probes for the kinetic coding (low biotin valency, mobile (M) probes; high biotin valency, immobile (I) probes).[19] For the optical coding, three different plasmonic nanostructures with distinctively different light scattering spectra [red (R), green (G), and blue (B) color-scattering nanostructures] were used (Figure 1a,b). Six types of optokinetically encoded NPs (MR-, MG-, MB-, IR-, IG-, and IB-NPs) were identified at single-particle level by real-time monitoring of their distinct scattering signals using dark-field microscopy (DFM). DNA sequences were modified to NP in a way that mobile NPs interact only with immobile NPs while M-NPs (or I-NPs) do not interact with other M-NPs (or I-NPs). It should be noted that target capturing induces assemblies of NPs and plasmonic coupling between NPs. The plasmonic coupling between different nanostructures generates unique scattering signal change, which is detectable and identifiable by DFM in a highly parallel manner (Figure 1b,d). Colorimetric signal change due to plasmonic coupling at the single nanoparticle-level was quantitatively analyzed with RGB color profiling method.

With this optokinetic (OK) coding strategy and highly photostable DFM-based single-particle analysis method on distinct plasmonic coupling, 9 different interactions between NPs induced by 9 different targets can be clearly distinguishable and detected on 2D SLB. Based on these designs and principles, we developed the OK-NP-tethered SLB (OK-NLB) assay. These nine NP assembly reactions were quantitatively analyzed as analogues of multicomponent association reactions (Figure 1c). Target miRNA sequences were selected based on the previous reports showing their abnormal expression patterns in multiple cancers.[20−22] In principle, one can potentially differentiate and diagnose prostate, breast, and lung cancers by identifying these 9 miRNA targets in one sample. The OK-NLB assay was further validated with HeLa cell-extracted total RNA samples for 9 different RNA sequences, and the results were compared to the qRT-PCR.

EXPERIMENTAL SECTION

Preparation of Small Unilamellar Vesicles (SUVs). The SLBs were formed on the lower cover glass by SUV vesicle fusion. The lipid in chloroform solution was mixed to have 97.2 mol % dioleoylphosphatidylcholine (DOPC), 0.3 mol % biotinylated dioleoylphosphatidylethanolamine (DOPE), and 2.5 mol % 1k poly(ethylene glycol)−DOPE. The lipid mixture was evaporated with a rotary evaporator, and the lipid film was thoroughly dried under a stream of nitrogen. The dried mixture was resuspended in deionized (DI) water and followed by three repetitive freeze−thaw cycles. The total lipid concentration was 2 mg/mL. The solution was extruded 31 times through a polycarbonate membrane with 100 nm pores at 25 °C. The SUV solution was kept at 4 °C until use.

Synthesis of Plasmonic Nanoparticles. Gold nanorods with an aspect ratio value of 4 were synthesized for red NPs by a seed-mediated growth mechanism. The seed was prepared by mixing 5 mL of 0.5 mM $HAuCl_4{\cdot}3H_2O$ solution with 5 mL of 0.2 M cetyltrimethylammonium bromide (CTAB), followed by rapid injection of 600 μL of ice-cooled 0.01 M $NaBH_4$ solution. The seed solution was kept for 2 h after the reducing step. A 5 mL aliquot of 0.5 mM $HAuCl_4{\cdot}3H_2O$ solution was mixed with 5 mL of 0.2 M CTAB solution, and 250 μL of 4 mM $AgNO_3$ solution was added, followed by 70 μL of 78 mM ascorbic acid solution. Seed solution (12 μL) was added and gently mixed. The solution was incubated for 4 h. To enhance scattering intensity, we coated the gold nanorods with thin silver shells. Gold nanorods (1 mL, 100 nM) were mixed with cetyltrimethylammonium chloride (1 mL, 10 mM), $AgNO_3$ (1 mL, 0.2 mM), and ascorbic acid (1 mL, 50 mM). After 4 h incubation, the solution was washed three times by centrifugation, supernatant removal, and redispersion in DI water. Spherical gold nanoparticles (50 nm) were purchased from BBI Solutions (Cardiff, UK) for nanoparticles scattering green light. To synthesize nanoparticles scattering blue light, we formed 20 nm silver shells on 20 nm gold seed. Two hundred microliters of mixture was prepared to obtain 150 pM of 20 nm gold nanoparticle (BBI Solutions, Cardiff, UK), 0.2% polyvinylpyrrolidone (PVP), and 0.25 mM $AgNO_3$. Sodium ascorbate solution (100 μL, 50 mM) was rapidly injected into the mixture to form a silver shell, and the color turned yellow immediately. This solution was directly used for DNA modification for particle stability. The TEM images are obtained using JEM-2100 (JEOL) systems at the National Center for Inter-University Research Facilities (NCIRF), Korea.

Preparation of OK-NPs. Synthetic thiolated oligonucleotides (Bioneer, Daejeon, Korea) were reduced by incubation with 100 mM dithiothreitol (DTT) in 100 mM phosphate buffer (PB) solution for 1 h and separated with an NAP-5 column (GE Healthcare, Buckinghamshire, U.K.). For detailed sequences of thiolated oligonucleotides attached on each OK-NP, see Table S3. The mixture of thiolated strands at a concentration of 4 μM were incubated with 50 pM plasmonic nanoparticles for 2 h at room temperature. The ratio of biotinylated strands to target capturing strands are 1%, 0.1%, 0.5%, and 30% for MR-NP, MG-NP, MB-NP, and I-NP, respectively. The solution was adjusted to 10 mM PB and 0.1% (w/v) sodium dodecyl sulfate. Three aliquots of 1 M NaCl and 0.01% sodium dodecyl sulfate (SDS) solution were added with 1 h interval between each addition to achieve a final concentration of 0.3 M. The mixture was heated at 55 °C for 10 min after each salt addition. The mixture was incubated overnight at room temperature. The suspension was washed by centrifugation, the supernatant removal, and particle redispersion in 10 mM PB solution three times.

Reaction Chamber Preparation. SLBs were formed inside a glass flow chamber, consisting of a top and bottom glass and a thermoplastic spacer. The top slide glass was drilled to form inlet and outlet holes and passivated with 10 mg/mL bovine serum albumin solution to block SLB formation. The bottom cover glass was sonicated for 10 min in chloroform, acetone, and DI water. After sonication, the bottom glass was cleaned with 1 M NaOH for 1 h and thoroughly washed with DI water. The top and the bottom glasses were assembled with a sandwiched thermoplastic spacer by heating at 120 °C on a digital hot plate. The SUV solution was prepared to have 1 mg/mL of SUV, 75 mM of NaCl, and 10 mM of phosphate buffer. The solution was introduced into the flow chamber for 40 min to form SLBs. The volume of the flow chamber was 9 μL. Streptavidin (10 nM) in 150 mM NaCl phosphate buffered saline (PBS, 10 mM phosphate buffer, pH 7.5) was injected to the flow cell to bind to the biotinylated lipid for 1 h. The flow cell was washed with 150 mM NaCl PBS twice at each step. NPs (1−10 pM) were reacted for 10 min to have optimized density of ∼700 NPs/14400 μm^2 for each M-NP and ∼1200 NPs/14400 μm^2 for each I-NP. The buffer was exchanged to 225 mM NaCl PBS for assay conditions.

Cell Culture. HeLa (human epithelial carcinoma line; ATCC, Num. CCL-2) cells were purchased from the Korean Cell Line Bank (Seoul, Korea). The cells were cultured in RPMI medium (Gibco, USA) containing 10% fetal bovine serum, 100 U/mL penicillin, and 100 μg/mL streptomycin (Gibco, USA). The cell line was incubated at 37 °C with 5% CO_2 in a humidified incubator.

Total RNA Extraction from HeLa Cells. We used the Qiagen miRNeasy miRNA extraction kit (Hilden, Germany), which isolates total RNA (>18 nucleotides) through phenol/guanidine-based lysis of samples and silica membrane-based purification. Eighty percent of confluent cells grown in a monolayer in 75 cm^2 flask were trypsinized and transferred to a clean 2 mL microcentrifuge tube. After centrifugation at 300 × *g* for 5 min, the cells were collected as a cell pellet, and the supernatant was completely aspirated. The cell pellet was mixed with 700 μL of QIAzol lysis reagent, homogenized by vortexing, incubated for 5 min at room temperature, and subsequently

DOI: 10.1021/jacs.7b01311
J. Am. Chem. Soc. 2017, 139, 3558−3566

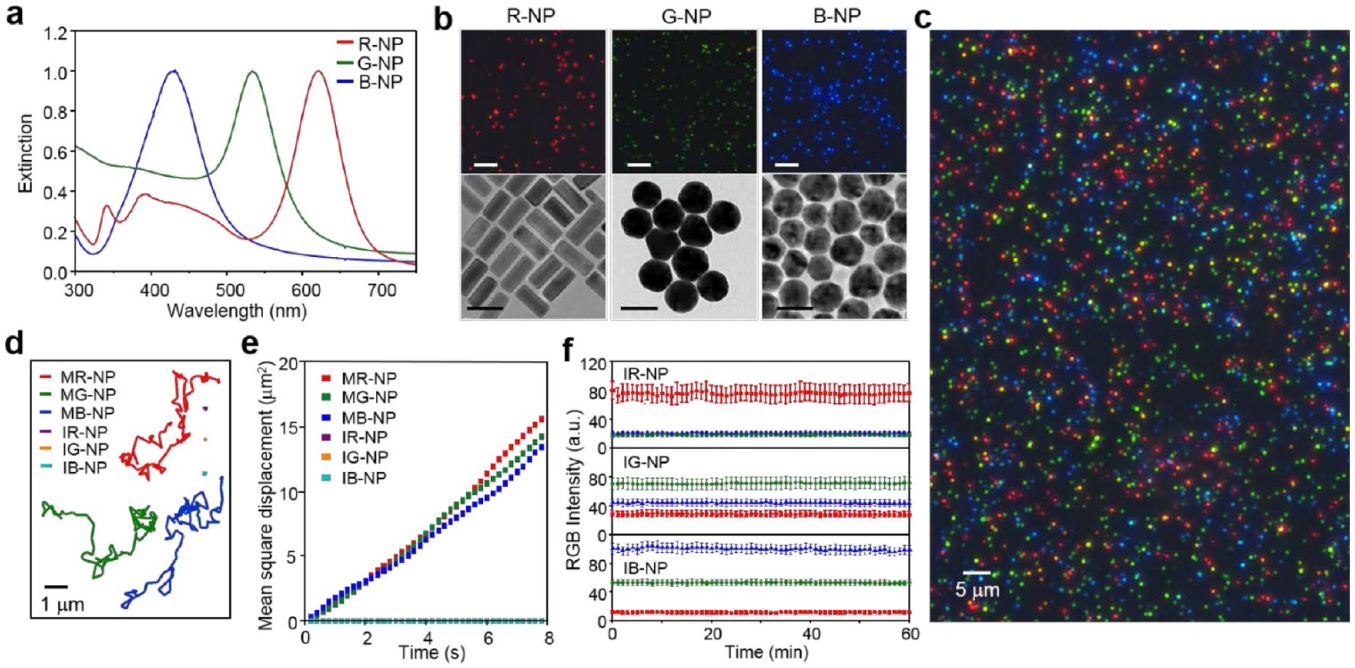

Figure 2. Photostable plasmonic NPs and DFM-based identification of the types of OK-NPs. (a) The extinction spectra of three optically encoded NPs. (b) DFM images (top) and transmission electron microscopy images (bottom) of R-NPs, G-NPs, and B-NPs (from left to right). The scale bars are 10 μm (DFM) and 50 nm (TEM). (c) A large area DFM image of the OK-NPs on SLB. (d) Representative diffusion trajectories and (e) mean square displacement plot of OK-NPs. The NPs with two kinetic states (M-NPs and I-NPs) show clear distinction in diffusion. (f) Averaged red (red square), green (green circle), and blue (blue triangle) scattering intensity of each I-NP under continuous dark-field illumination for 60 min. The images were taken every 1 min, and error bars are standard deviation from 20 NPs.

mixed with 140 μL of chloroform. The organic and aqueous phases were separated by centrifugation for 15 min at 12 000 × g at 4 °C. The aqueous phase containing the RNA was carefully transferred to a new collection tube and mixed with 1.5 volumes of 100% ethanol. The mixture was loaded into an RNeasy Mini spin column and washed several times at 8100 × g. The RNeasy Mini column was transferred to a clean 1.5 mL collection tube, and RNA was eluted by addition of 50 μL of RNase-free water. The total RNA concentration was 120 ng/μL with A_{260}/A_{280} = ~2. The cell extract was kept frozen until use.

Real-Time Monitoring of Combinatorial Assembly between OK-NPs and OK-NLB Assays. The movement and combinatorial assembly between OK-NPs on SLBs were observed with DF microscope (Axiovert 200M, Carl Zeiss, Germany) with 40× objective lens (NA = 0.6) and AxiCam HR color camera. To characterize association of OK-NPs and to obtain a calibration curve, synthetic miRNAs were purchased from Bioneer (Daejeon, Korea) (Table S3). Known concentrations of miRNA targets in 225 mM NaCl PBS were injected into the reaction chamber. The negative control sample contains 300 pM of miR-100. The NP binding events were monitored with DFM. Snapshot images were taken at 10 min intervals for 1 h, and the assembly events in a 120 × 120 μm^2 area were counted. It should be noted that the calibration curves for detection targets of interest need to be calculated only one time, and the preobtained calibration curves can be used for actual assays. For the HeLa cell assay, cell extracts were diluted to a final concentration of 600 ng/μL in 225 mM NaCl PBS and injected into the reaction cell. Three replicate samples were analyzed. The images were analyzed using ImageJ software (https://imagej.nih.gov/ij/).

qRT-PCR Analysis. The qRT-PCR analysis of cell extracts was performed using Geno-Total RNA kit (Genolution, Seoul, Korea). cDNA was synthesized from total RNA sample with the Mir-X kit (Clontech). A SYBR Green-based qRT-PCR reaction was conducted with the real-time PCR system (Bio-Rad CFX) using Geno-qPCR kit no. RD1101 (Genolution, Seoul, Korea). PCR was carried out with initial denaturation at 95 °C for 2 min, followed by 40 cycles of 95 °C for 5 s and 60 °C for 20 s. Relative expressions of each miRNA to U6 snRNA as an internal control were calculated by the $2^{-\Delta CT}$ method. The reactions were run in duplicate to obtain standard deviations.

RESULTS AND DISCUSSION

In a typical experiment, we prepared DNA-modified nanoparticles and tethered these particles to SLBs. Three target capture DNA sequences that are half-complementary to target miRNA, were modified onto each OK-NPs (Figure 1 and Table S3). For distinct optical encoding, we prepared three types of plasmonic nanoparticles that scatter red, green, and blue light by varying size, shape, and composition to yield desirable optical properties. Gold nanorods with a silver shell (~46 nm in longer axis and ~13 nm in shorter axis with ~5 nm shell), gold nanospheres (~47 nm in diameter), and silver nanospheres on gold seeds (~19 nm core and ~37 in diameter) were synthesized and used as R-NPs, G-NPs, and B-NPs, respectively. The DFM images showed red, green, and blue scattering signals from the nanoparticles, and R-NPs, G-NPs, and B-NPs showed distinct localized surface plasmon resonance at different wavelengths in the extinction spectra (Figures 2a,b). Because of their distinct optical properties, we can individually identify R-, G-, and B-NPs from a mixture of densely tethered NPs on SLBs (Figure 2c). The NPs were kinetically encoded on the SLB by controlling the ratio of biotinylated (tethering group to streptavidin) DNA to target-capturing DNA on the nanoparticle surface. Biotinylated DNA can be bound to the biotinylated SLB via multivalent streptavidin linkers. The particles with a low valency were tethered with high mobility, whereas the particles with a high valency were immobilized by forming multiple linkages between the particles and the SLB.[19] M-NPs showed random 2D Brownian motion confirmed by linear mean square displacement plot (Figures 2d,e). Nearly 90% of M-NPs were mobile on the SLB (Figure S1a). The

DOI: 10.1021/jacs.7b01311
J. Am. Chem. Soc. 2017, 139, 3558−3566

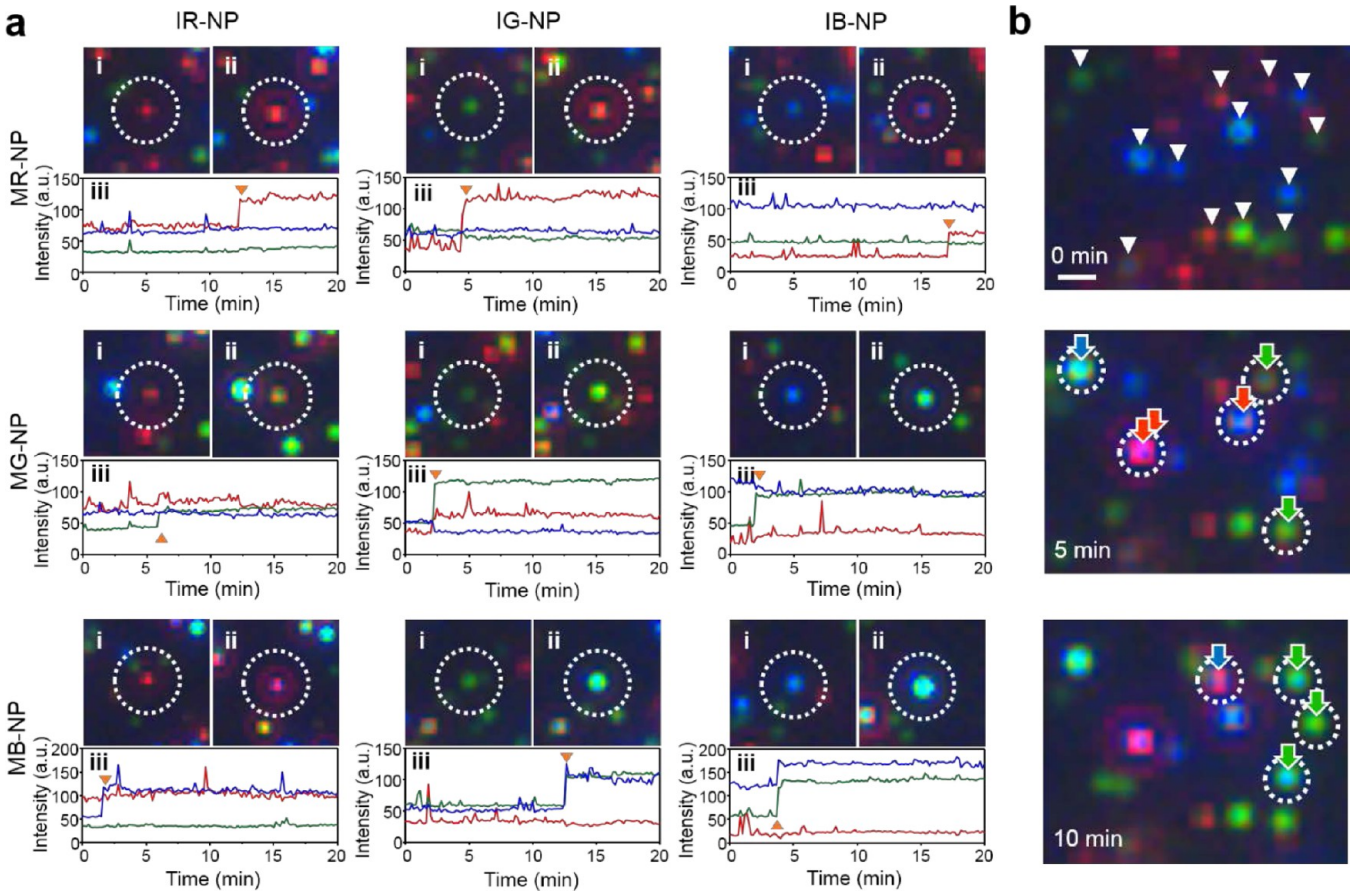

Figure 3. Multiplexable and parallel identification of the interaction between OK-NPs by combinatorial plasmonic coupling. (a) Real-time monitoring of combinatorial assemblies between OK-NPs. OK-NPs were monitored with 10 s interval after addition of 10 nM of 9 target miRNAs. DFM images of 9 combinations at (i) 0 min and (ii) 20 min (Videos S1−9). The bindings of M-NPs to I-NPs result in distinct color and signal intensity change. (iii) The RGB intensity profiles show characteristic patterns for the binding of MR-, MG-, and MB-NPs. The binding events are indicated with orange triangles. (b) Parallel observation of the individual binding events (white dashed circle) between I-NPs (white triangle) and MR- (red arrow), MG- (green arrow), and MB-NPs (blue arrow) (Video S10). The scale bar is 1 μm.

lipid-tethered NPs occasionally exhibited a confined behavior and hop diffusion when observed for a prolonged period (>10 min), mainly because of incomplete homogeneity in lipid substrates.[23] Particle diffusion in fluids is explained by the Stokes−Einstein equation, which describes that hydrodynamic radius is inversely proportional to diffusion coefficients in 3D Brownian motion. Interestingly, the average diffusion coefficients of MR-, MG-, and MB-NPs were 0.362 ± 0.227, 0.383 ± 0.203, and 0.379 ± 0.202 $\mu m^2/s$, respectively. These results indicate that the diffusion of these mobile probes did not depend on the different hydrodynamic size of the NPs, which implies that the diffusion of the tethered NPs is mainly driven by the lateral mobility of lipids, and the kinetic encoding of NPs is decoupled with optical encoding. We also checked the photostability of OK-NPs on SLBs under continuous illumination of dark-field light source for 1 h (Figure 2f). Significantly, the RGB profiles of scattering intensities of red, green, and blue probes were well maintained without photoblinking or photobleaching for the whole observation period (60 min), indicative of high photostability of the light-scattering OK-NPs on SLB. Next, we verified that the real-time monitoring of the six OK-NPs can differentiate 9 different types of plasmonic coupling signals based on different target miRNA-induced binding events (Figure 3a and Videos S1−9). Without target addition, only transient scattering color changing events were observed due to temporary nonspecific overlaps between M-NPs and I-NPs. In the presence of the targets, the miRNAs were hybridized with half complementary DNA strands on both M- and I-NPs, confining M-NPs to I-NPs to induce plasmonic coupling between particles. We interpreted and classified the types of association events using light-scattering signal changes in DFM images and RGB intensity profiles of each particle. R-, G-, and B-NP monomers were represented as distinct red, green, and blue spots in the DF image with the strongest red, green, and blue channel intensities, respectively, in RGB profiles (Figure S1b). Binding of MR-, MG-, and MB-NPs to an I-NP increased red, green, and blue color intensities, respectively. Accordingly, the red, green, and blue colors of R−R, G−G, and B−B homodimers are significantly brighter than R-, G-, and B-NP monomers. The R−G, G−B, and B−R heterodimers displayed orange, cyan, and magenta colors. The binding of a MR-NP to an I-NP only increased red color intensity with negligible changes in green and blue color intensities. Assembly with MG-NPs enhanced both red and green color intensities, whereas assembly with MB-NPs resulted in distinct change in blue color intensity. A red-shift of color profile in association among G- and B-NPs was observed as a result of a plasmonic coupling effect.[24] The formations of MG−IG dimer and MB−IB dimer induced higher R to G and G to B ratios, respectively, compared to their monomer states. The

DOI: 10.1021/jacs.7b01311
J. Am. Chem. Soc. 2017, 139, 3558−3566

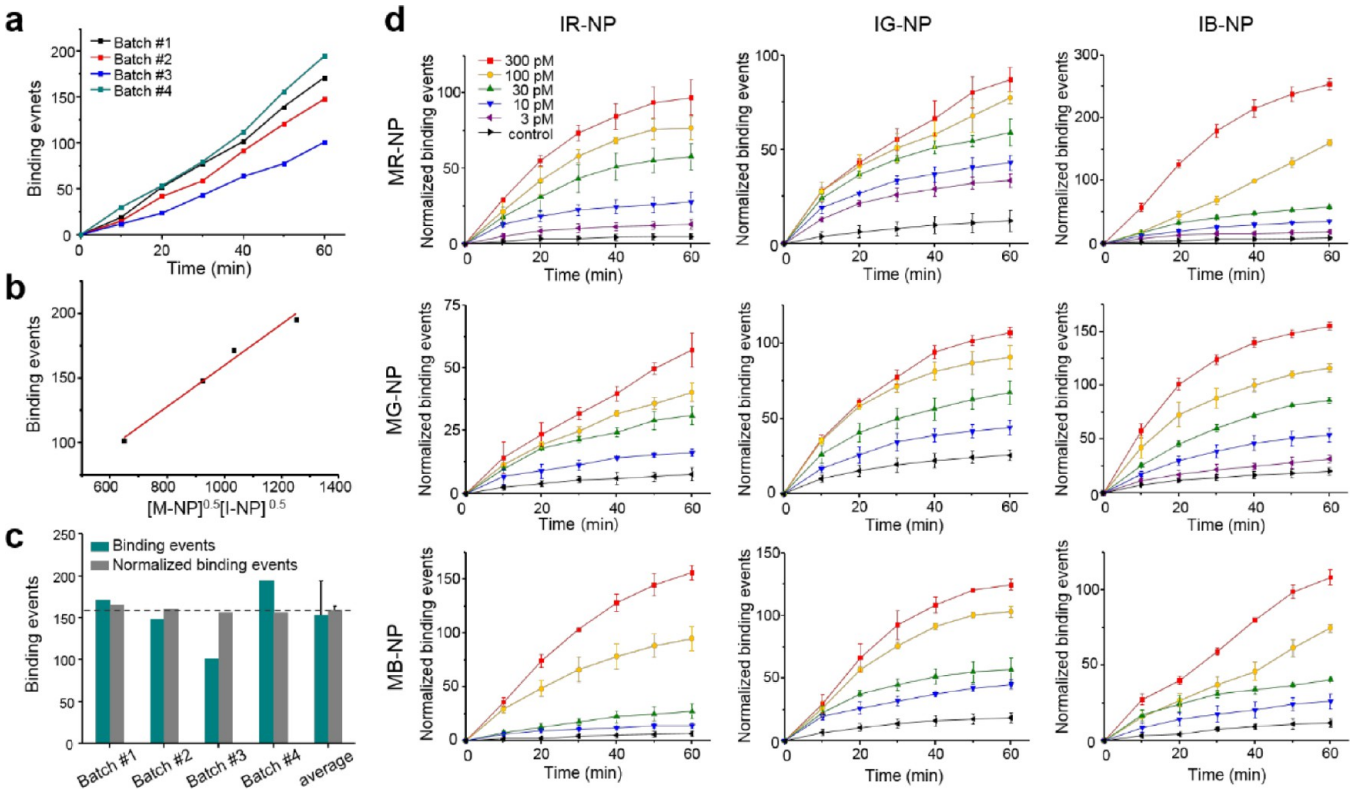

Figure 4. Kinetics and quantification of miRNA binding events. (a) Cumulative binding events for 60 min between MR-NPs and IB-NPs at 100-pM miRNA with different NP densities on SLB (Table S1). (b) The number of binding events at 60 min is proportional to $[\text{M-NP}]^{0.5}$ and $[\text{I-NP}]^{0.5}$. The orders were fitted to have the largest R^2 value (0.9868) and the smallest standard deviation of normalized binding events. (c) Binding events at 60 min from different batches were normalized by (normalized binding events) $= \frac{(\text{binding events})}{[\text{M-NP}]^{0.5}[\text{I-NP}]^{0.5}} \times 1000$ NPs/unit area was set as an internal reference. The normalized binding events with varying NP densities show similar values with a small standard deviation compared to the standard deviation without normalization. (d) Normalized binding events of 9 miRNAs at different concentrations. The error bars represent the standard deviations from three independent experiments. Control experiments contained 300 pM of negative control miRNA (miR-100).

above *in situ* monitoring and color profiling strategy also can identify trimer formation (the addition of a third NP to dimer). However, in the case of tetramer formation (addition of the fourth NP to trimer, which is rare), it was challenging to differentiate which M-NP was engaged with the trimer, due to the complex plasmonic coupling arising from different geometric configurations. Therefore, we controlled the density of I-NPs to be higher than that of M-NPs to reduce multimer formation and thereby simplify data analysis. Due to heterogeneity in the size and optical signals of NPs, particle tracking should be initiated prior to the target addition to fully differentiate each NP assembly event with high reliability. All 9 types of different interactions were successfully discriminated and counted in a parallel manner over a large area (Figure 3b and Video S10).

Before obtaining a calibration curve, we analyzed the NP reaction kinetics. The binding events can be regarded as multicomponent association reactions (Figure 1c and eq 1).

$$\text{I-NP} + \text{M-NP} + \text{miRNA} \rightarrow \text{I–M complex} \quad (1)$$

We first tested the effect of NP density on NP association reaction. Although we aimed to load a similar number of NPs on SLBs in different reaction chambers by controlling loading time and particle concentration, there were deviations in the NP density for each batch. The higher density of M-NPs and I-NPs resulted in an increased number of binding events for the same target concentration (Figure 4a and Table S1). When the number of binding events after 60 min incubation was proportional to $[\text{I-NP}]^{0.5}[\text{M-NP}]^{0.5}$, the lowest standard deviation and largest R^2 value were obtained (Figure 4b).

The logarithm of target concentration showed a linear behavior with the normalized binding events (Figure S2). By considering the NP density and target concentration factors, we can build the reaction kinetics equation for the OK-NP reaction.

$$\text{binding events} = k_{\text{XY}} \frac{[\text{IX-NP}]^{0.5}[\text{MY-NP}]^{0.5}}{1000\text{NPs/unit area}}$$
$$\log([\text{miRNA}]/\text{pM}) \quad (\text{X, Y} = \text{R, G, B}) \quad (2)$$

where k_{XY} is reaction rate constant (1 h), which represents the binding efficiency, [IX-NP] and [MY-NP] is the 2D NP density. To remove the effect of different NP density per reaction chamber, we used the normalized the binding events by setting the internal reference as 1000NPs/unit area with the density factor after measurement (eq 3 and Figure 4c).

$$\text{normalized binding events} = (\text{binding events}) \frac{1000\text{NPs/unit area}}{[\text{I-NP}]^{0.5}[\text{M-NP}]^{0.5}} \quad (3)$$

We calculated the k values for nine different OK-NP reactions with the slope of a linear relation region of the calibration curve (Figure S2 and Table S2). Considering melting temperature of

DOI: 10.1021/jacs.7b01311
J. Am. Chem. Soc. 2017, 139, 3558–3566

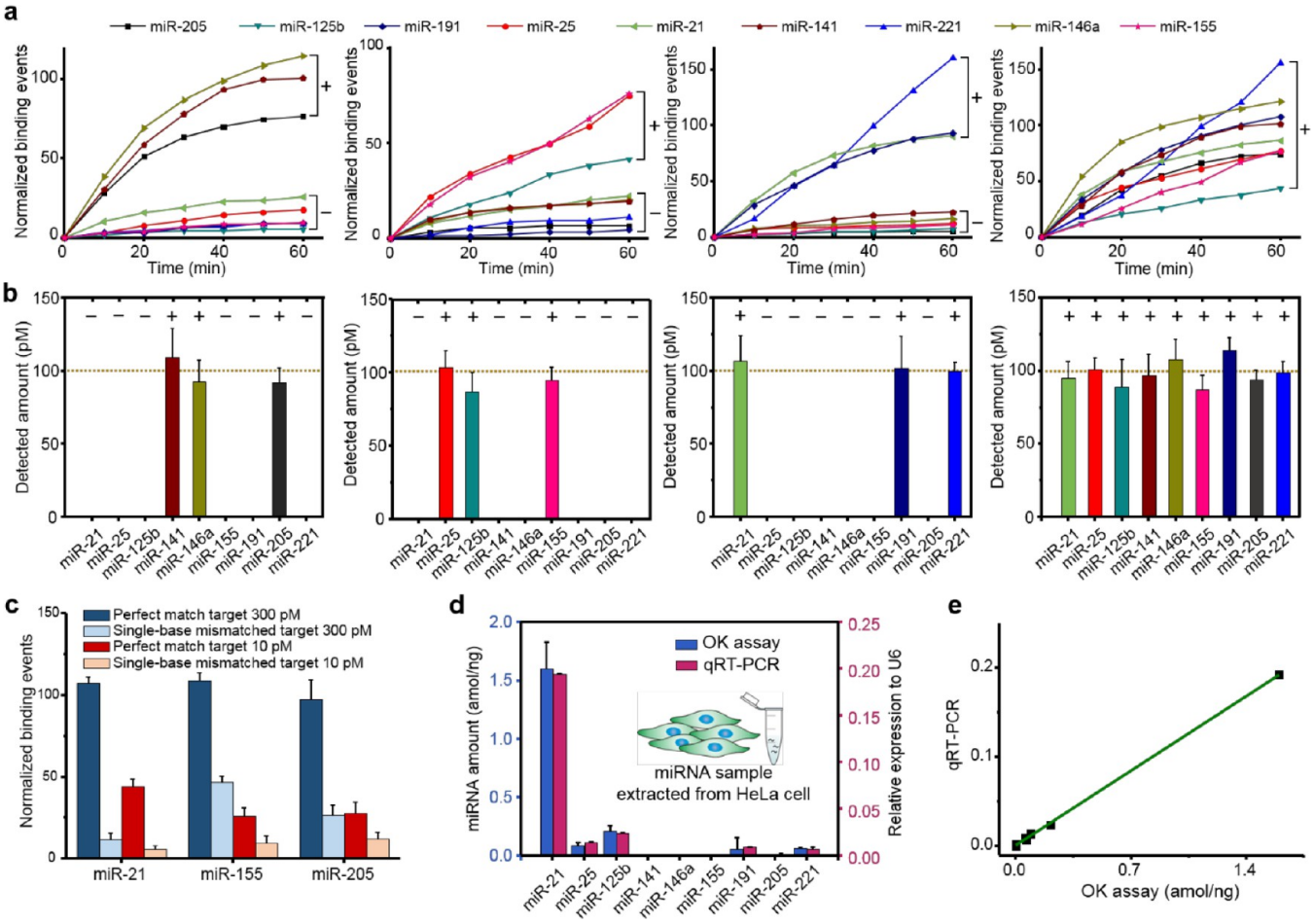

Figure 5. Multiplexed detection of miRNA sequences. (a) Representative data for *in situ* monitoring of binding events and (b) multiplexed profiling results from different combinations of 100 pM target miRNA sequences. Plus (minus) sign indicates presence (absence) of the target miRNA in samples. The detected amount was obtained from calibration curves (Figure S2). The dashed lines indicate the added amount of target miRNA. The results prove the multiplexing capability and negligible cross-reactivity within experimental errors of the assay. (c) Discrimination between target miRNA and single-base-mismatched target at 300 and 10 pM. Single-base-mismatched target shows <43% normalized binding events at 300 pM and indistinguishable signals from control signals at 10 pM. (d) Multiplexed miRNA profiling of total RNA extract from HeLa cells and validation with qRT-PCR. qRT-PCR result shows relative expression value to U6 snRNA. (e) Correlation of OK-NLB assay with qRT-PCR based on the results of total RNA from HeLa cells. The 9 target miRNA results obtained with two methods show a strong agreement (R^2 = 0.9993). The standard deviations are obtained from three independent experiments.

a target sequence, the association reaction between R-NP and B-NP shows the highest value. The rate constant is affected by the hybridization energy, which is determined by the target miRNA sequence, DNA modification density for OK-NPs, NP morphology, etc. The diversity in k value implies that the target sequence and the types of NPs affect the binding efficiency.

Under these conditions, we obtained the calibration curves of the normalized binding events with target concentrations ranging from 3 to 300 pM (Figure 4d). The binding events were counted on 120 × 120 μm^2 SLBs with consecutive images every 10 min. The logarithm of target concentration showed linear behavior with the normalized binding events (Figure S2). The limit of detection (LoD) ranged between 3 and 10 pM (30−100 amol) for 9 miRNA targets without optimizations. The kinetic responses of binding events were dependent on the combination of NPs. Furthermore, miRNA sequence has an influence on the kinetics of assembly and disassembly with complementary DNA sequences.[25]

An assay time of 1 h was sufficient to discriminate different target concentrations. Longer assay time did not noticeably increase the sensitivity because the binding event curve reached a plateau after 1 h when a small amount of target was present. OK-NLB assay allows for differentiating small differences in miRNA expression, which is key to distinguishing dysregulated miRNA expression for cancer diagnosis.[13]

To examine the multiplexing capability and the cross-reactivity of the OK-NLB assay, we tested samples containing 100 pM targets with several different combinations of miRNA targets (Figures 5a,b). miRNA profiling results were analyzed through *in situ* monitoring of nine association reactions. Although each M-NP is designed to bind to three types of I-NPs simultaneously, the assay showed negligible cross-reactivity in all the cases and specifically detected the targets with high reliability and quantification capability. Even when all 9 targets existed in one sample, the assay was able to detect all the targets with similar quantification results (the far right histogram of Figure 5b). We also confirmed the specificity of the assay. Single-base-mismatched targets at 300 and 10 pM were tested for three orthogonal targets (miR-21 for MG-IG, miR-155 for MB-IB, and miR-205 for MR-IR; Figure 5c and Table S3). The single-base-mismatched target showed <43% signal intensities of the signals for 300 pM perfectly matched DNA case. The

DOI: 10.1021/jacs.7b01311
J. Am. Chem. Soc. 2017, 139, 3558−3566

signals from 10 pM single-base-mismatched targets were not differentiable from control signals. The single nucleotide polymorphism (SNP) in G−C pair for miR-205 showed greater discrimination than SNP in A−U pair for miR-21. The detected amount of 300 pM single-base mismatched input ranged between 10 and less than the LoD. The results prove the SNP selectivity and specificity of the OK-NLB assay.

Finally, we performed miRNA profiling of total RNA samples extracted from HeLa cells (human cervical adenocarcinoma) with the OK-NLB assay (Figure 5d). We used 0.6 μg of total RNA for cancer cell assay. miR-21, an oncogene widely overexpressed in diverse cancers including cervical cancers,[26] showed the highest expression level. The measured values of miR-141, miR-146a, miR-155, and miR-205 were below LoD, and this result is consistent with the previous report that showed those miRNAs have low or no expression in HeLa cells.[27] We spiked miR-146a (30 pM final concentration) in a total RNA sample and quantified it using the OK-NLB assay. The detected amount of target was 25.7 ± 1.62 pM. The spiked sample showed 94% of the normalized binding events, compared to that of the same concentration of target sample in buffer condition. Six percent signal loss was largely due to cell debris in the lysate observed on the SLB (Figure S3). We further validated the result of the OK-NLB assay using qRT-PCR. The relative expression value of each miRNA to the internal reference U6 was plotted against the absolute concentration of miRNA obtained from OK-NLB assay (Figure 5e). The two assay results showed strong agreement with R^2 values of >0.999. Moreover, the expression pattern of 9 miRNA targets was well matched with the reported value obtained by microarray-based assay.[28]

CONCLUSION

In summary, we developed an optokinetically encoded light-scattering NP-based assay on SLBs (OK-NLB assay), which allows real-time monitoring of individual NP assembly modes. The assay enables rapid, sensitive, quantitative, and multiplexed profiling of 9 different miRNAs in one sample without complicated setup, target modification, and enzymatic amplification. The probes on SLBs used herein were modified with three different target miRNA complements and mobility-controlling biotinylated DNA for multiplexed optokinetic encoding and showed remarkable photostability with DFM that allows for *in situ* monitoring of the probes and reliable quantification of their binding events with miRNA. As a proof of concept, we showed the highly specific detection of various combinations of 9 different miRNA targets with 9 interacting pairs of probes between mobile R, G, or B probes and immobile R, G, or B probes on SLBs. *In situ* single-particle monitoring and normalized RGB analysis of 2D diffusion and target miRNA-facilitated binding of a large number of the photostable NPs with DFM in a highly parallel manner allows for reliably differentiating and quantifying 9 different miRNA targets in one sample. Moreover, single-base mismatched target miRNA sequences were clearly discernible from target miRNA sequences on the OK-NLB assay platform. Highly selective detection of different miRNA sequences used here implies the diagnosis of breast, prostate, lung, pancreas and stomach cancers from clinical samples could be potentially possible with further optimizations.[9] For rigorous validation, we profiled the expression levels of 9 miRNAs from cervical cancer cell extracts within 1 h and confirmed that the expression pattern is consistent with qRT-PCR result. The assay should be readily applicable to study other complex biological and chemical reactions because the surface of OK-NPs can be modified with diverse biochemical ligands.[28−30] The multiplexed profiling strategy with OK-NPs on SLBs expands the number of multiplexable targets and opens new ways of developing highly multiplexed signals with photostable probes on a highly analyzable, quantifiable platform. The OK-NLB platform could be useful for rapid and multiplexed pathogen detection,[31,32] as well as cancer diagnosis.

ASSOCIATED CONTENT

Supporting Information

Videos of combinatorial assemblies of OK-NPs with dark-field microscopy. The Supporting Information is available free of charge on the ACS Publications website at DOI: 10.1021/jacs.7b01311.

Characterization of OK-NPs, binding events dependence on the number of OK-NPs, calibration curve of OK-NLB assay, monitoring of cell debris during cell assay, detailed sequence of oligonucleotides. (PDF)

Video 1 of combinatorial assemblies between MR-NP and IR-NP with dark-field microscopy (MP4)

Video 2 of combinatorial assemblies between MR-NP and IG-NP with dark-field microscopy (MP4)

Video 3 of combinatorial assemblies between MR-NP and IB-NP with dark-field microscopy (MP4)

Video 4 of combinatorial assemblies between MG-NP and IR-NP with dark-field microscopy (MP4)

Video 5 of combinatorial assemblies between MG-NP and IG-NP with dark-field microscopy (MP4)

Video 6 of combinatorial assemblies between MG-NP and IB-NP with dark-field microscopy (MP4)

Video 7 of combinatorial assemblies between MB-NP and IR-NP with dark-field microscopy (MP4)

Video 8 of combinatorial assemblies between MB-NP and IG-NP with dark-field microscopy (MP4)

Video 9 of combinatorial assemblies between MB-NP and IB-NP with dark-field microscopy (MP4)

Video 10 of multiparallel observation of combinatorial assemblies between OK-NPs with dark-field microscopy (MP4)

AUTHOR INFORMATION

Corresponding Author

*jmnam@snu.ac.kr

ORCID

Jwa-Min Nam: 0000-0002-7891-8482

Present Address

†Y.-K.L.: Department of Chemistry, University of California, Berkeley, California, USA.

Notes

The authors declare no competing financial interest.

ACKNOWLEDGMENTS

This work was supported by Samsung Research Funding & Incubation Center of Samsung Electronics under Project Number SRFC-MA1502-02 and the National Research Foundation of Korea (NRF) grant funded by the Korea government (MSIP) (No. 2016R1A2A1A05005430).

DOI: 10.1021/jacs.7b01311
J. Am. Chem. Soc. 2017, 139, 3558−3566

REFERENCES

(1) Milo, R.; Shen-Orr, S.; Itzkovitz, S.; Kashtan, N.; Chklovskii, D.; Alon, U. *Science* **2002**, *298*, 824−827.
(2) Bray, D. *J. Theor. Biol.* **1990**, *143*, 215−231.
(3) Grzybowski, B. A.; Bishop, K. J. M.; Kowalczyk, B.; Wilmer, C. E. *Nat. Chem.* **2009**, *1*, 31−36.
(4) Carregal-romero, S.; Caballero-Díaz, E.; Beqa, L.; Abdelmonem, A. M.; Ochs, M.; Hühn, D.; Suau, B. S.; Valcarcel, M.; Parak, W. J. *Annu. Rev. Anal. Chem.* **2013**, *6*, 53−81.
(5) Zhao, Y.; Cheng, Y.; Shang, L.; Wang, J.; Xie, Z.; Gu, Z. *Small* **2015**, *11*, 151−174.
(6) He, L.; Hannon, G. J. *Nat. Rev. Genet.* **2004**, *5*, 522−531.
(7) Mitchell, P. S.; Parkin, R. K.; Kroh, E. M.; Fritz, B. R.; Wyman, S. K.; Pogosova-Agadjanyan, E. L.; Peterson, A.; Noteboom, J.; O'Briant, K. C.; Allen, A.; Lin, D. W.; Urban, N.; Drescher, C. W.; Knudsen, B. S.; Stirewalt, D. L.; Gentleman, R.; Vessella, R. L.; Nelson, P. S.; Martin, D. B.; Tewari, M. *Proc. Natl. Acad. Sci. U. S. A.* **2008**, *105*, 10513−10518.
(8) Li, Y.; Kowdley, K. V. *Genomics, Proteomics Bioinf.* **2012**, *10*, 246−253.
(9) Wang, J.; Zhang, K. Y.; Liu, S. M.; Sen, S. *Molecules* **2014**, *19*, 1912−1938.
(10) Carthew, R. W.; Sontheimer, E. J. *Cell* **2009**, *136*, 642−655.
(11) Pritchard, C. C.; Cheng, H. H.; Tewari, M. *Nat. Rev. Genet.* **2012**, *13*, 358−369.
(12) Lee, H.; Park, J.-E.; Nam, J.-M. *Nat. Commun.* **2014**, *5*, 3367.
(13) Wang, Y.; Zheng, D.; Tan, Q.; Wang, M. X.; Gu, L.-Q. *Nat. Nanotechnol.* **2011**, *6*, 668−674.
(14) Degliangeli, F.; Kshirsagar, P.; Brunetti, V.; Pompa, P. P.; Fiammengo, R. *J. Am. Chem. Soc.* **2014**, *136*, 2264−2267.
(15) Alhasan, A. H.; Kim, D. Y.; Daniel, W. L.; Watson, E.; Meeks, J. J.; Thaxton, C. S.; Mirkin, C. A. *Anal. Chem.* **2012**, *84*, 4153−4160.
(16) Lu, N.; Gao, A.; Dai, P.; Song, S.; Fan, C.; Wang, Y.; Li, T. *Small* **2014**, *10*, 2022−2028.
(17) Dong, H.; Zhang, J.; Ju, H.; Lu, H.; Wang, S.; Jin, S.; Hao, K.; Du, H.; Zhang, X. *Anal. Chem.* **2012**, *84*, 4587−4593.
(18) Zeng, Y.; Zhu, G.; Yang, X.; Cao, J.; Jing, Z.; Zhang, C. *Chem. Commun.* **2014**, *50*, 7160−7162.
(19) Lee, Y. K.; Kim, S.; Oh, J. W.; Nam, J. M. *J. Am. Chem. Soc.* **2014**, *136*, 4081−4088.
(20) Volinia, S.; Calin, G. a; Liu, C.-G.; Ambs, S.; Cimmino, A.; Petrocca, F.; Visone, R.; Iorio, M.; Roldo, C.; Ferracin, M.; Prueitt, R. L.; Yanaihara, N.; Lanza, G.; Scarpa, A.; Vecchione, A.; Negrini, M.; Harris, C. C.; Croce, C. M. *Proc. Natl. Acad. Sci. U. S. A.* **2006**, *103*, 2257−2261.
(21) Wang, W.-T.; Chen, Y.-Q. J. *J. Hematol. Oncol.* **2014**, *7*, 86.
(22) Kosaka, N.; Iguchi, H.; Ochiya, T. *Cancer Sci.* **2010**, *101*, 2087−2092.
(23) Hsieh, C. L.; Spindler, S.; Ehrig, J.; Sandoghdar, V. *J. Phys. Chem. B* **2014**, *118*, 1545−1554.
(24) Rong, G.; Wang, H.; Skewis, L. R.; Reinhard, B. M. *Nano Lett.* **2008**, *8*, 3386−3393.
(25) Johnson-Buck, A.; Su, X.; Giraldez, M. D.; Zhao, M.; Tewari, M.; Walter, N. G. *Nat. Biotechnol.* **2015**, *33*, 730.
(26) Lu, Z.; Liu, M.; Stribinskis, V.; Klinge, C. M.; Ramos, K. S.; Colburn, N. H.; Li, Y. *Oncogene* **2008**, *27*, 4373−4379.
(27) Nelson, P. T.; Baldwin, D. A.; Scearce, L. M.; Oberholtzer, J. C.; Tobias, J. W.; Mourelatos, Z. *Nat. Methods* **2004**, *1*, 155−161.
(28) Xianyu, Y.; Xie, Y.; Wang, N.; Wang, Z.; Jiang, X. *Small* **2015**, *11*, 5510−5514.
(29) Chen, W.; Cao, F.; Zheng, W.; Tian, Y.; Xianyu, Y.; Xu, P.; Zhang, W.; Wang, Z.; Deng, K.; Jiang, X. *Nanoscale* **2015**, *7*, 2042−2049.
(30) Zhou, W.; Gao, X.; Liu, D.; Chen, X. *Chem. Rev.* **2015**, *115*, 10575−10636.
(31) Hauck, T. S.; Giri, S.; Gao, Y.; Chan, W. C. W. *Adv. Drug Delivery Rev.* **2010**, *62*, 438−448.
(32) Hu, R.; Liu, T.; Zhang, X. B.; Huan, S. Y.; Wu, C.; Fu, T.; Tan, W. *Anal. Chem.* **2014**, *86*, 5009−5016.

DOI: 10.1021/jacs.7b01311
J. Am. Chem. Soc. 2017, 139, 3558−3566